Reconstruction of Low Dimensional Electronic States by Altering the Chemical Arrangement at the $SrTiO_3$ Surface

Li, Hang; Brito, Walber H.; Guedes, Eduardo B.; Chikina, Alla; Dahm, Rasmus T.; Christensen, Dennis V.; Yun, Shinhee; Chiabrera, Francesco M.; Plumb, Nicholas C.; Shi, Ming

Total number of authors:
12

Published in:
Advanced Functional Materials

Link to article, DOI:
10.1002/adfm.202210526

Publication date:
2023

Document Version
Publisher's PDF, also known as Version of record

Citation (APA):
Li, H., Brito, W. H., Guedes, E. B., Chikina, A., Dahm, R. T., Christensen, D. V., Yun, S., Chiabrera, F. M., Plumb, N. C., Shi, M., Pryds, N., & Radovic, M. (2023). Reconstruction of Low Dimensional Electronic States by Altering the Chemical Arrangement at the $SrTiO_3$ Surface. *Advanced Functional Materials*, *33*(19), Article 2210526. https://doi.org/10.1002/adfm.202210526

ADVANCED FUNCTIONAL MATERIALS
www.afm-journal.de

Reconstruction of Low Dimensional Electronic States by Altering the Chemical Arrangement at the $SrTiO_3$ Surface

Hang Li, Walber H. Brito, Eduardo B. Guedes, Alla Chikina, Rasmus T. Dahm, Dennis V. Christensen, Shinhee Yun, Francesco M. Chiabrera, Nicholas C. Plumb, Ming Shi, Nini Pryds, and Milan Radovic**

Developing reliable methods for modulating the electronic structure of the 2D electron gas (2DEG) in $SrTiO_3$ is crucial for utilizing its full potential and inducing novel properties. Herein, it is shown that relatively simple surface preparation reconstructs the 2DEG at the $SrTiO_3$ (STO) surface, leading to a Lifshitz-like transition. Combining experimental methods, such as angle-resolved photoemission spectroscopy (ARPES) and X-ray photoemission spectroscopy with ab initio calculations, that the modulation of the surface band structures can be effectively achieved via transforming the chemical composition at the atomic scale is found. In addition, ARPES experiments demonstrate that vacuum ultraviolet light can be efficiently employed to alter the band renormalization of the 2DEG system and control the electron-phonon interaction . This study provides a robust and straightforward route to stabilize and tune the low-dimensional electronic structure via the chemical degeneracy of the STO surface.

1. Introduction

Transition metal oxide-based interfaces and surfaces, in particular those based on STO, exhibit a plethora of properties such as superconductivity,[1–5] magnetism,[6–9] Rashba-type spin-orbital coupling,[10,11] and quantum Hall effect.[12,13] $SrTiO_3$, with a cubic perovskite structure, is a typical choice as a substrate for epitaxial growth of many oxides. In cubic STO, the octahedral crystal field splits the Ti 3*d* orbitals in the well-known t_{2g} and e_g subbands, with degenerate t_{2g} states at the Γ point and the e_g states lying at higher energies. Structural relaxation and reconstructions at the STO surface and interface regions can lift the degeneracy and lower the dimensionality of the electronic bands.[14] The evolution of the electronic phases in STO-based systems and its relation to the properties have been intensively investigated:, e.g., high mobility in γ-Al_2O_3/STO,[15,16] anomalous Hall effect induced by Lifshitz transition,[17] quantum Hall effect,[12,13] and Rashba-like spin structure.[18,19] The mentioned complex phenomena, which often coincide, demonstrate that understanding the electronic structure and the low degeneracy surface is crucial to understanding the causes of these behaviors and achieving control over them. Because of its simplicity, studies on the bare $SrTiO_3$ surface are essential to shed light on the fundamental mechanisms leading to the observed band order and predicting new ways for their manipulation.

The band structure in bare STO and related interfaces can be modified by temperature change,[20–23] stress,[24–26] surface termination,[27–29] and oxygen vacancies.[30] ARPES studies on nominally TiO_2-terminated STO single crystal [14,31,32] display the typical electronic structures of STO consisting of shallow d_{xz}/d_{yz} bands and deep d_{xy} subbands – a fingerprint of most STO-based systems. Interestingly, a single band was observed in the epitaxially grown SrO layer on TiO_2-terminated STO.[27] Intriguingly, a recent study of SrO-capped STO systems exhibits the absence of electronic states near E_F.[34] This lack can arise due to the surface insensitive nature of soft X-ray incident light used for this study, which is unfavorable to detecting the d_{xy} surface band in Sr-enriched STO. However, all of these studies suggest that the surface termination and its chemical composition play a crucial role in determining the properties of the underlying 2DEG.

Figure 1 shows a schematic illustration of two possible surfaces terminations of STO (001) (TiO_2 and SrO) and their combination (Figure 1a) as well as their electronic structures (Figure 1c).[14,18,26,27,31,32] If the octahedral symmetry of the

H. Li, R. T. Dahm, D. V. Christensen, S. Yun, F. M. Chiabrera, N. Pryds, M. Radovic
Department of Energy Conversion and Storage
Technical University of Denmark
2800 Kgs. Lyngby, Denmark
E-mail: hang.li@psi.ch; milan.radovic@psi.ch

H. Li, E. B. Guedes, A. Chikina, N. C. Plumb, M. Shi, M. Radovic
Photon Science Division
Paul Scherrer Institute (PSI)
5232 Villigen, Switzerland

W. H. Brito
Departamento de Física
Universidade Federal de Minas Gerais
C. P. 702, Belo Horizonte, MG 30123–970, Brazil

The ORCID identification number(s) for the author(s) of this article can be found under https://doi.org/10.1002/adfm.202210526.

DOI: 10.1002/adfm.202210526

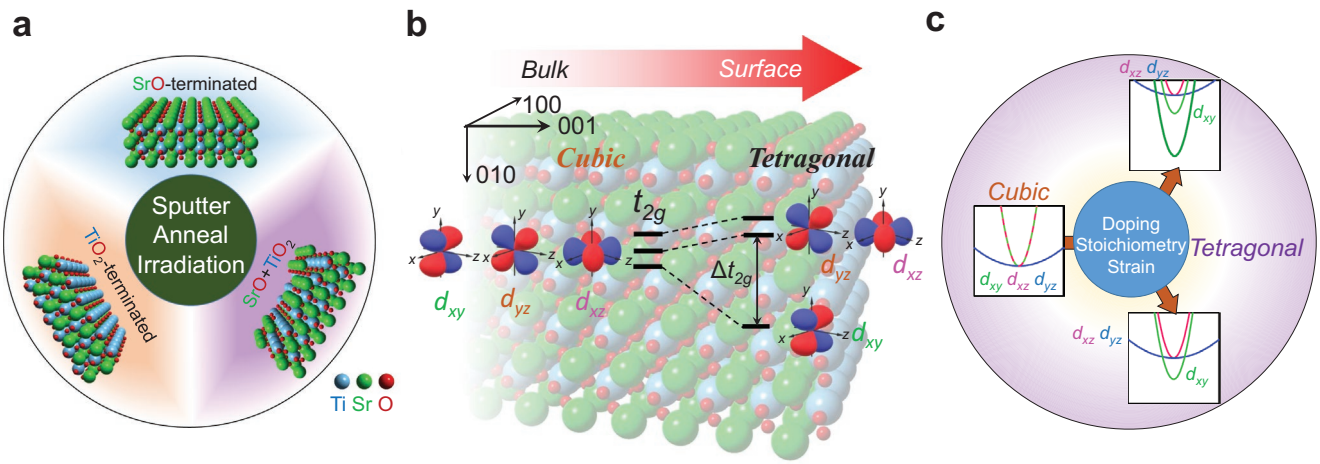

Figure 1. a) Schematic illustration of $SrTiO_3$ surfaces with three types of terminations, SrO-termination, TiO_2-termination and SrO+TiO_2-termination, respectively. b) Tetragonal crystal field splitting between d_{xy} and d_{xz}/d_{yz} bands, where Δt_{2g} marks the energy difference. c) Schematic illustration of the electronic structures of STO surfaces observed in our study.

001-oriented STO is preserved at the surface, it protects the degeneracy of the t_{2g} (d_{xy}, d_{xz} and d_{yz}) bands. Lowering the symmetry from octahedral to tetragonal leads to splitting of the d_{xy} and the d_{xz}/d_{yz} bands (Figure 1b), characterized by the energy difference, Δt_{2g}. We have used this parameter to evaluate the lowering of dimensionality and the degeneracy of Nb-doped STO wafers through surface engineering. Furthermore, it was shown that increasing temperature causes a depletion of the 2DEG of STO [23] while reducing the orbital splitting, which can be further controlled by strain.[26]

By combining Ar sputtering and vacuum annealing, we establish a vigorous procedure to tune the 2DEG of STO (Figure 1c). Importantly, we report that the 2D d_{xy} subband emerges at a Sr-enriched surface, leading to a pure single-orbital 2DEG system. This electronic phase is found to be air-stable, offering an advantage for applications. Meanwhile, the band splitting between d_{xy} and d_{xz}/d_{yz} caused by ultraviolet (VUV) irradiations demonstrates that light can be used as a knob for tuning the band splitting (Δt_{2g}) and Lifshitz-like transition in the 2DEG system.

2. Results and Discussion

2.1. Band Structures of Surface-Engineered STO

Figure 2 displays the electronic structures of STO single crystal (001) surfaces measured by ARPES after various preparation processes. The as-received STO samples are nominally TiO_2-terminated with 0.5% Nb doping (SurfaceNet GmbH). The characterizations of the "as-received" sample (stage #1) were performed by ARPES and XPS and used as reference. Subsequently, the sample was treated by a mild Ar sputtering and annealing (stage #2: 5 min of Ar sputtering followed by annealing in ultra-high vacuum (UHV) at 700 °C for 1 h). Afterward, we annealed the sample at 800 °C for 2 h in UHV (stage #3). Both stages (#2 and #3) were studied by XPS and ARPES. The detailed surface preparation procedure is presented in the Methods section and in Figure S1 (Supporting Information).

The ARPES data in Figure 2 were obtained using circular polarized (C+) light. With such light polarization, both in-plane d_{xy} and out-of-plane d_{xz}/d_{yz} orbitals at the STO surface are probed,[20–22] showing the evolution of the electronic structure during irradiation. Figure 2a–c display the electronic structures of STO in stages #1, #2, and #3 after 100 min of irradiation along the Γ-X direction. Similar to previous ARPES studies on STO surfaces,[14,31–33] the electronic structures of as-received STO (#1) and high-temperature annealed STO (#3) after irradiation of t_f~1.6 h show degenerate d_{xz} and d_{yz} bands and down-shifted d_{xy} subbands (Figure 2a,c). The band structure measurement of stage #2 (Figure 2b) shows that only one d_{xy} subband near the Γ point is occupied. This indicates an electronic transition from a multi-band (#1) to a single-band system (#2) and back (#3).

The band character of stages #1 to #3 is depicted by in-plane Fermi surfaces (FSs) maps and k_z maps (Figure 2j–l). For stages #1 and #3 (Figure 2j,l), the in-plane FSs consist of one circular electron pocket and two intersecting ellipsoidal electron pockets centered at Γ, which are typical for the STO (001) surface.[14,31,32] The d_{yz} and d_{xz} bands for stages #1 and #3 exhibit quasi-3D characters, while the d_{xy} band shows 2D character (Figure 2j,l). In contrast, stage #2 is characterized only by a single circular electron pocket around Γ (Figure 2k) with 2D character –, i.e., without dispersion in the k_z direction (Figure 2k). The occupation of a single band was earlier reported in the LAO/STO [17] and STO systems.[19,27] However, in the following section, we will discuss the origin and properties of the single d_{xy} band with pure 2D character found in stage #2.

2.2. Surface Chemical Composition and Theoretical Analyses

Figure 3a and b present XPS spectra of the STO sample in the three stages by measuring the Sr 3d and Ti 3p and Ti 2p core levels with photon energies in the VUV (170 eV; surface

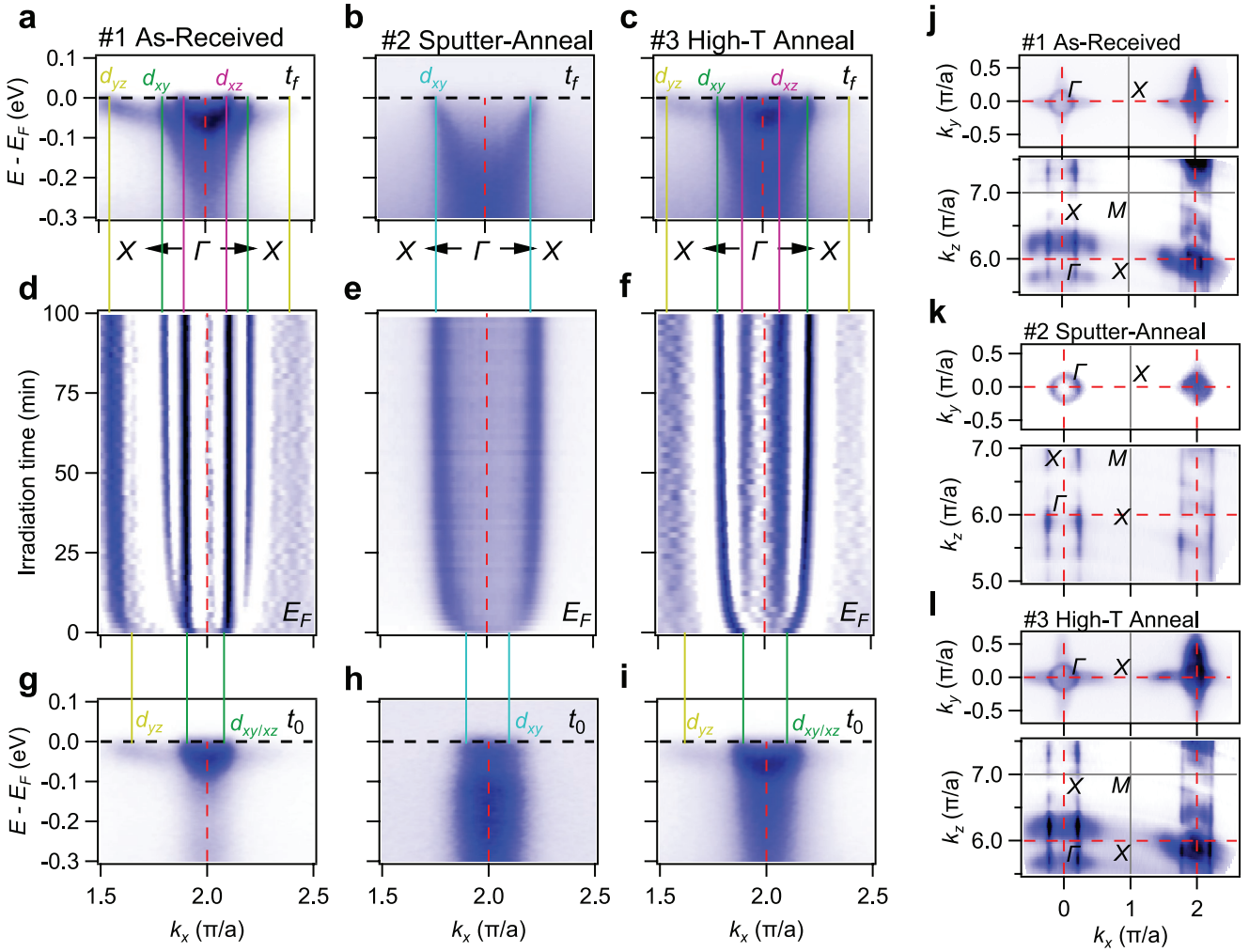

Figure 2. a–c) ARPES intensity cuts of as-received (stage #1), sputter-annealed (stage #2), and high temperature annealed (stage #3) STO wafers, respectively, after saturating the carrier density by irradiation (t_f). d–f) k-resolved ARPES maps at E_F of stages #1 to #3, respectively, as a function of VUV irradiation time. e) is an intensity map, and d,f are horizontal 2nd derivative maps. g–i) ARPES intensity cuts of stages #1 to #3 measured at a fresh spot and acquired within 2 min of VUV-irradiation (t_0), respectively. Green, pink, cyan, and yellow lines mark the k_F of d_{xy}, d_{xz}, d_{xy} in #2, and d_{yz} bands, respectively. j–l) Fermi surface maps of the ΓXY plane (upper) by in-plane mapping and the ΓXZ plane (lower) by $h\nu$-dependent mapping of stage #1 to #3, respectively. Grey solid lines mark the Brillouin zone boundary and red dashed lines show the high-symmetry lines. Figure a–i and the upper panel of j–l are measured at 85 eV. All figures are measured with circular polarized (C+) light.

sensitive) and soft X-ray (750 eV; more bulk sensitive) ranges. In the regions of the spectra where core-levels of Ti are situated, the peaks at binding energy (E_B) E_B~38 eV (3p) (Figure 3a) and at E_B~459 eV (2p) (Figure 3b) are due to Ti^{4+} ions, while the peaks at E_B~35 eV and at E_B~457 eV belong to the Ti^{3+} ions. The overall shape of Ti^{4+} is similar for all stages, while in stage #3 we have observed a minor amount of Ti^{3+} as compared to the other two (Figure 3b), which could be presumably due to the sputter-induced oxygen vacancies. Yet a remarkable transformation happens with Sr 3d core level of STO surface after sputtering and annealing (#2). While the data acquired by soft X-rays (Figure 3b) do not show the effect of the heat treatment, the VUV-XPS data reveals that the spectral weight of Sr at the surface is significantly raised (Figure 3a). Moreover, the same data show that the additional annealing (in #3) transforms the doublet peaks of the Sr 3d core level into a multipeak (at least two doublets) structure, indicating the presence of chemically distinct Sr species after surface rearrangement.

By comparing the spectral weight of Sr 3d and Ti 3p core levels using VUV light (surface sensitive) for stages #1 and #2, it is evident that surface treatment yields an increased Sr content. Interestingly, with additional annealing (stage #3), the opposite trend was observed: the spectral weight of Sr 3d decreases while the weight of Ti 3p increases. To quantify this effect, we use the ratio of Sr and Ti (I_{Sr}/I_{Ti}) spectral weight (integral one) of the three stages obtained from the VUV and soft X-ray data, as shown in Figure 3c. We set the Sr/Ti ratio of as-received STO (stage #1) to unity and normalized the other values to it. As a result, the ratio I_{Sr}/I_{Ti} of the surface region (VUV-extracted) increases by ≈50% from stage #1 to stage #2 and decreases in stage #3. In contrast, the ratio I_{Sr}/I_{Ti} of the bulk-like region (soft X-ray extracted) remains nearly

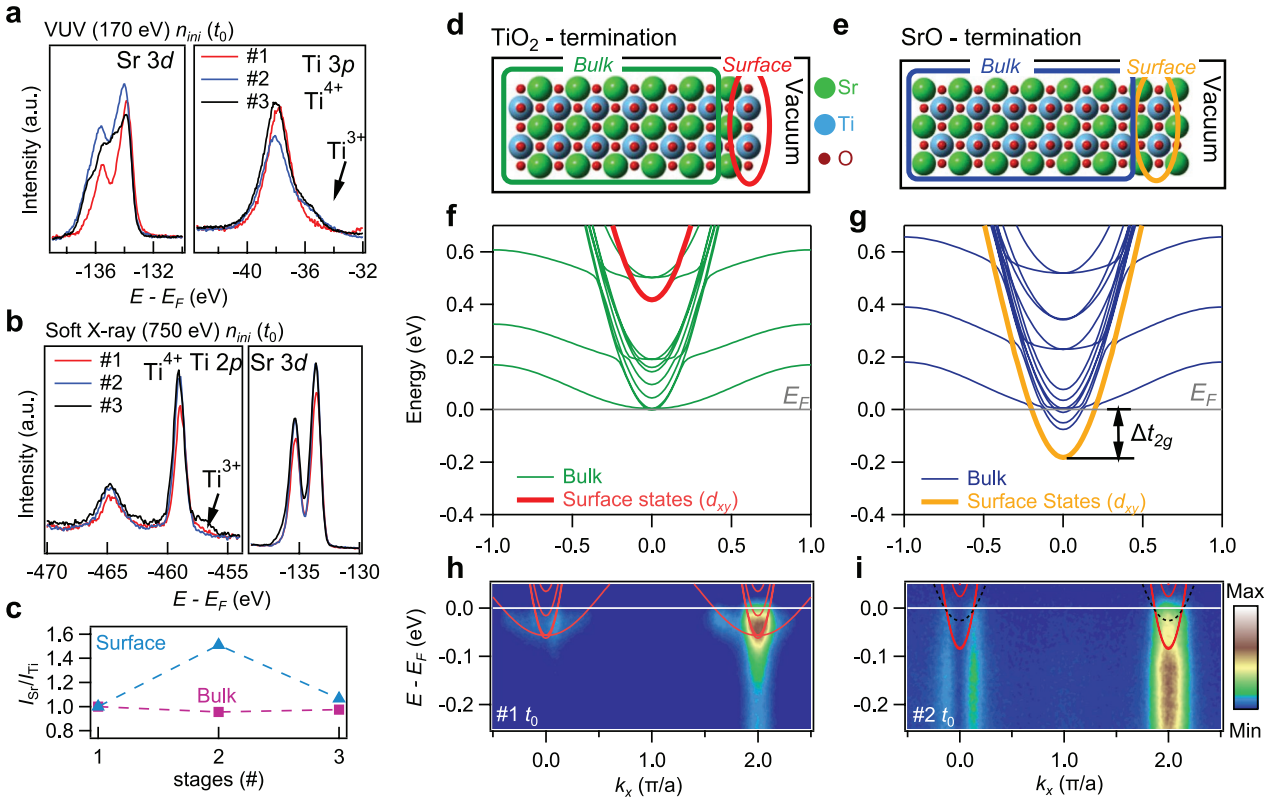

Figure 3. a,b) Core-level of Ti 3*p* and Sr 3*d* orbitals measured at $h\nu = 170$ eV at the initial carrier density of the three stages (t_0). b) Core-level of Ti 2*p* and Sr 3*d* orbitals measured at 750 eV at the initial carrier densities of the three stages (t_0). c) Calculated spectral weight ratio of Sr/Ti extracted from a and b, and normalized to the ratio of the as-received STO wafer (#1). d,e) Relaxed 2 × 2 × 7 STO slabs of TiO_2-termination and SrO-termination, respectively. Red/orange ellipses and dark green/blue squares mark the superficial TiO_2 layer and the bulk of the two models, respectively. Green, blue, and red spheres represent the Sr, Ti, and O atoms, respectively. f,g) Calculated electronic band structures of TiO_2- and SrO- terminated STO models as presented in a and b, respectively. The red and orange curve in f and g highlights the d_{xy} band from the first TiO_2 layer. h,i) ARPES intensity cuts of as-received (#1) and sputter-annealed (#2) STO wafer at t_0, plotted with calculated band structures (red curves) in f and g, respectively. The calculated bands are rigidly shifted to match the carrier densities. The dashed black curves in i show the fitted d_{xy} bands.

unchanged. The obtained results suggest that the surface preparation alters the surface chemical composition from a nominally TiO_2-terminated surface (#1) to one with increased Sr content (#2). Additional annealing seems to restore the TiO_2 termination. S. N. Rebec et al. reported that the SrO layer deposited on TiO_2-terminated STO yields a similar one-band electronic feature.[27] Furthermore, the same study showed that the I_{Sr}/I_{Ti} ratio also increases by ≈50% for the SrO-capped sample,[27] similar to our result presented in Figure 3c. However, these results indicate that the surface chemical composition can be utilized as a knob for modulating the electronic structures of the STO surface. The full set of XPS data and detailed analyses of core levels and chemical states can be found in Supporting Information Section VI.

To resolve the link between the STO surface composition and the band reconstruction, we employ theoretical calculations of TiO_2- and SrO- terminated STO to emulate the two possible final derivatives of surface preparation (Figure 3d,e). In our studies, we define the splitting parameter, Δt_{2g}, as the energy difference between the lowest d_{xy} and d_{xz}/d_{yz} states instead of the energy splitting between the t_{2g} states from the first TiO_2- layer. Represented in this way, Δt_{2g} experimentally measured by ARPES can be compared with ones obtained from the slab calculation (the detailed band structures with orbital projections and structural parameters can be found in Supporting Information Section III). For the TiO_2-terminated STO slab, the calculation shows that the band splitting (Δt_{2g}) between d_{xy} band bottom and d_{yz}/d_{xz} band bottom is negligible (Figure 3f). This outcome is, indeed, in good agreement with band structures observed in stage #1 at t_0 (Figure 2g), indicating that the cubic symmetry is mostly preserved (Figure 3h). In contrast, the calculations for SrO-terminated slabs show that the d_{xy} band (derived from the first TiO_2 layer under SrO surface layer, which is highlighted in Figure 3g) shifts downward with ≈150 meV, generating the splitting of t_{2g} bands with tetragonal symmetry. Indeed, the ARPES data for stage #2 (t_0) reveals this type of 2D band, which is slightly shallower than the calculated one (Figure 3i). A possible explanation for this deviation is the larger effective mass of the observed band (t_0) caused by the strong EPI, which was not considered in the theoretical calculations. When the E_F is set according to the

experimental k_F (Figure 3h,i), only the surface d_{xy} band crosses E_F for #2, while the other t_{2g} bands remain unoccupied, hence showing that a single-band state arises in stage #2.

Although we show here that the termination yields a clear distinction in the surface electronic structure (regarding the surface state), oxygen vacancies can still affect it, causing a transfer of the 2D to 3D electronic structure.[35] Nevertheless, the amount of oxygen vacancies might differ in both, SrO-terminated and TiO_2-terminated surfaces or mixed ones. Indeed, it was reported that a SrO-termination completely inhibits the incorporation of oxygen vacancies at the surface.[36] Consequently, the absence of oxygen vacancies in the SrO top layer can result in different lattice distortion, band structure, and surface doping of the STO surface compared to TiO_2 terminated. Previous work of Juan Shen et al.[37] has addressed the effects of a large concentration of oxygen vacancies (OVs) on the band structure of STO slab for different terminations and using an asymmetric simple slab model. This study showed that OVs are the possible cause of the 2D electronic structure at STO surface. However, our structural model used for DFT is a symmetric slab for both surface terminations, where all the atom's position and lattice parameters were optimized. This approximation avoided the appearance of any artificial dipole produced within the supercell. As a result, our DFT calculations validate the finding based on photoemission experiments: the Sr-enriched STO (001) surface is characterized by the intrinsic splitting of the t_{2g} states and the surface state, producing a pure 2D electronic structure. Therefore, the surface state with d_{xy} character, which is first occupied when the system is doped, should be considered the main component of the 2DEG system.[27,28,38]

2.3. Wedge-Potential in STO

One of the key parameters of the STO band structures, shown in Figure 2, is the splitting of the d_{xy} and d_{xz}/d_{yz} bands (Δt_{2g}). E. B. Guedes et al., by combining DFT calculation and ARPES, established the link between atomic displacements of STO surface layers and Δt_{2g}.[23] However it is experimentally observed that Δt_{2g} alters during beam irradiation (Figure 2d,f) and directly correlates to carrier density.

Starting as a degenerate system (Figure 2g,i), the d_{xy} and d_{xz}/d_{yz} bands separate (Figure 2d,f) later during irradiation, resulting in 3D d_{xz}/d_{yz} bands and 2D d_{xy} subbands (Figure 2a and c). The extracted Fermi momenta (k_F) and the energy splitting between d_{xy} and d_{xz}/d_{yz} bands (Δt_{2g}) as a function of irradiation time illustrate this process more clearly (see also Figure S6f, Supporting Information). It has been extensively discussed in the literature that the STO-based 2DEG system experiences a wedge-like potential within the surface region.[31,36,38] This potential at the STO surface can be described using a quantum well model with the form, $V(z) = V_0+eFz$, where F is the strength of the electric field in the direction perpendicular to the sample surface, and e is the charge of the electron (**Figure 4**a). The quantized eigenenergies (E_n) of subbands at the surface region can be described by:[31,40]

$$E_n = V_0 + \left(\frac{\hbar}{2m_z^*}\right)^{1/3}\left[\left(\frac{3\pi}{2}\right)\left(n-\frac{1}{4}\right)eF\right]^{2/3} \quad (1)$$

where m^*_z is the effective mass along the field direction (perpendicular to the surface).

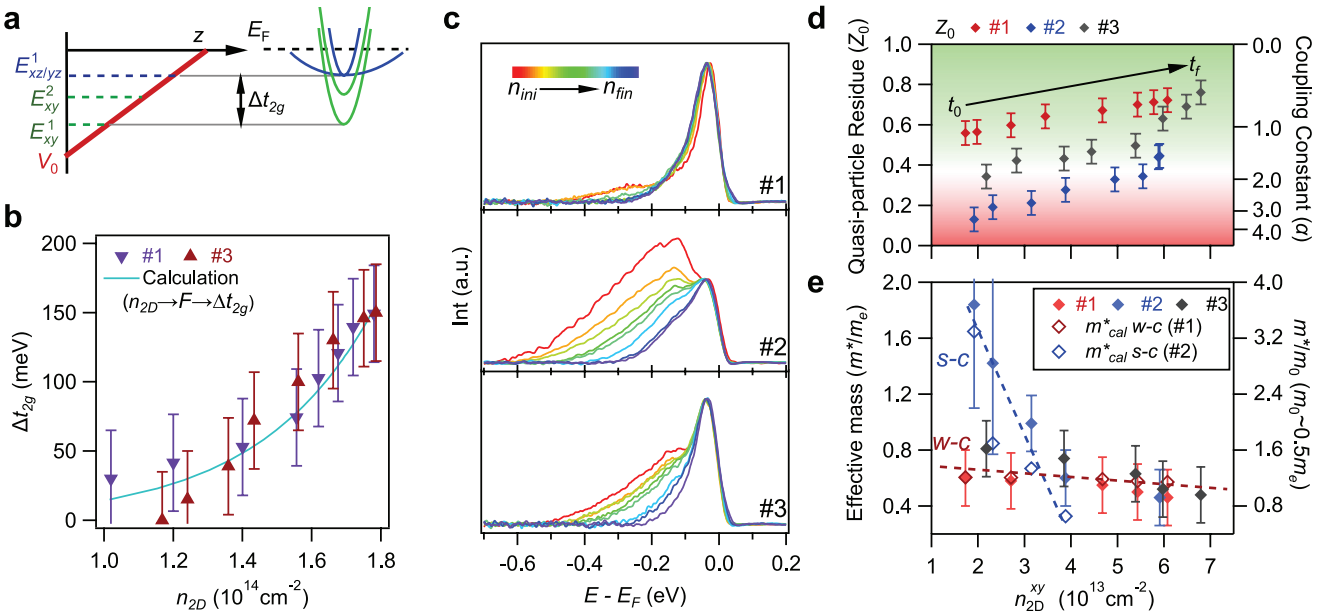

Figure 4. a) Illustration of wedge potential and band structure at the surface of STO. b) Calculated energy differences between d_{xy} and d_{xz}/d_{yz} bands (Δt_{2g}) as a function of carrier density, and experimental Δt_{2g} extracted from ARPES data of stages #1 and #3. c) Energy distribution curves of stage #1 to #3 at different carrier densities at $k = k_F^{xy}$. d) Calculated quasiparticle residue (Z_0) from the EDCs (presented in panel a) as a function of carrier density of d_{xy} bands, n_{2D}^{xy}. The gradient background and right axis indicate the transition between weak (light green) to strong (light red) coupling strength (reproduced from reference [42]). e) Fitted effective masses of d_{xy} bands of all three stages as a function of n_{2D}^{xy}. The empty marks represent the calculated effective mass from coupling strength (α) by weak-coupling, $m^*/m_0 = 1/(1-\alpha/6)$, and strong coupling, $m^*/m_0 = 0.0232\alpha^4$, of Fröhlich polarons, respectively.

The band splitting of t_{2g} bands, Δt_{2g}, can be calculated by the difference between the $n = 1$ eigenenergies of d_{xy} and d_{xz}/d_{yz} bands as $\Delta t_{2g} = E_1^{xy}\text{-}E_1^{xz/yz}$ in the following way:

$$\Delta t_{2g} = 7.5\times10^{-7}\left[\left(\frac{m_e}{m_z^{*xz/yz}}\right)^{1/3} - \left(\frac{m_e}{m_z^{*xy}}\right)^{1/3}\right]F^{2/3} \quad (2)$$

The relationship between F and the carrier density (n_{2D}) can be describe in the following way:[40]

$$\frac{e}{2}n_{2D} = \int_0^F \varepsilon_0\ \varepsilon_r\left(F'\right)dF' \quad (3)$$

(ε_0: the vacuum dielectric constant; $\varepsilon_r(F)$: is field-dependent dielectric constant of STO) From Equation 3 it is possible to extract the electric field by using the carrier densities of each band taken from the ARPES data (See Figure S6f,g, Supporting Information Section IV). The effective mass m^*_z of d_{xy} and d_{xz}/d_{yz} bands can also be estimated by ARPES.

Figure 4b shows the calculated and experimental values of Δt_{2g} of stages #1 and #3 as a function of the carrier density, n_{2D}. The agreement between the observed and calculated values of Δt_{2g} indicates that the electric field (F or $\varepsilon_r(F)$) is caused by the accumulation of charges at the surface during the irradiation process.

As mentioned above, the free charge density (directly measured by ARPES) is one of the parameters that can establish the link between the density and the Δt_{2g} splitting. However, free charges probably originate from the oxygen vacancies (as donors), photo-doping, or both. Since the d_{xz}/d_{yz} bands are invisible by ARPES (laying above Fermi level) in the SrO-terminated one, we can only use the experimentally obtained Δt_{2g} for the TiO_2 terminated surface.

At least two possibilities can be considered as the causality of t_{2g} splitting: 1) the intrinsic, due to tetragonal distortion, and 2) the extrinsic, which happens due to the illumination during the ARPES experiment. Indeed, the wedge potential well describes the second scenario depicting that the splitting depends on the carrier density of free charges (See Figure 4a,b).

Our calculations show that the structural relaxation of the SrO- terminated STO slab causes more significant polarization (and the field), yielding the intrinsic splitting in t_{2g} states (Supporting Information Section III). Consequently, the free charges can be accumulated and trapped near the surface with such a field, forming the conducting states. Moreover, additional carriers (generated during ARPES experiments) might cause an alteration of a polarization profile. Indeed, the study by Delugas and coworkers [38] showed that the t_{2g} splitting gains when the carrier densities increase, leading to a similar band structure as the wedge potential model shows.

However, all our analysis implies that the lattice distortion[23] cooperates vigorously with the field (generated by free electrons), conducting to the common properties of the 2DEG at the STO surface.

2.4. EPI and Effective Mass

The waterfall-like feature identified as an incoherent part of the band dispersion (see Figure 2g,h) is usually attributed to the polaronic electron-phonon interaction (EPI) in STO, which plays an essential role in modulating the physical properties of the 2DEG.[41–43] The EPI can be quantified by the quasi-particle (QP) residue, $Z_0 = I_{QP}$ / ($I_{QP} + I_{hump}$), where the $I_{QP/hump}$ represents the integrated spectral weight of QP/hump of corresponding energy distribution curves (EDCs).[43,44]

Figure 4c displays the background-subtracted EDCs of stages #1-3 taken at the k_F of the d_{xy} bands for different carrier densities, $n(t)$, normalized by the QP peak's intensity. The peak-dip-hump line shape, which extends to higher binding energy (Figure 4c), relates to the multiple phonon modes interacting with electrons.[43,44] However, the EPI at t_0 (red curves in Figure 4c), related to intrinsic transport properties, exhibits a significant increase for stage #2 (a reduction of Z_0 from 0.55 in #1 to 0.15 in #2) and partially recovers after the sample has been additionally annealed (Z_0~0.35 in #3). Therefore, besides changes in the band topology (see Figure 2), surface engineering also modifies the EPI strength, affecting the carrier properties such as the effective mass, m^* (from $0.6m_e$ in #1 to $1.8m_e$ in #2, and $0.8m_e$ in #3, See Figure S8, Supporting Information). Figure 4d shows the EPI strength (through Z_0) as a function of the carrier densities of d_{xy} bands. The positive (negative) Z_0 (EPI) behavior for different carrier densities is probably due to the screening suppressing the long-range Fröhlich polaron interaction.[41,43] It is important to note that the spectral weight of the peak-dip-hump structures undergoes a continuous decrease during irradiation, indicating a weakening of the EPI for all stages (#1 to #3).

In weak coupling and long-range electron-phonon interactions, the relationship between effective mass and quasiparticle residue (Z_0) is defined by the Fröhlich model, where the effective mass of the electrons is enhanced due to EPI: $m^*/m_0 = 1/(1\text{-}\alpha/6)$, m_0 is the bare band mass, and α is the coupling strength,[45,46] which can be estimated from Z_0 by a diagrammatic quantum Monte Carlo study (presented in Figure 4d with a gradient background and the right axis).[47] In Figure 4e, we plot both the effective mass fitted from the band dispersion (fitting details are presented in Supporting Information Section IV and V) and the one calculated one from Z_0 by weak-coupling Fröhlich model of stages #1 as a function of carrier density. Our data show good agreement between the fitted m^* and calculated values for stages #1 and #3 for all observed carrier densities. However, for stage #2 this concurrence is valid only for the high doping regime, which is consistent with the weak coupling regime (See Figure 4d, and more details are shown in Figure S9, Supporting Information). For the low-doping regime of stage #2, with $Z_0 < 0.3$ and $\alpha > 3$ (Figure 4d), a strong coupling model we used for the approximation established by R. P. Feynman,[48] $m^*/m_0 = 0.0232\alpha^4$, which reproduces the effective mass more appropriately, as shown in Figure 4e.

Our data and analyses in Figure 4e and d show that the EPI transits from the weak coupling (stage #1) to the strong coupling regime (stage #2). Further, the verified inverse relation between the EPI strength and the effective mass of all three stages shows the softening of polarons caused by increasing carrier densities.[41]

3. Summary and Outlook

Employing systematic XPS measurements, we show that combining Ar sputtering and UHV annealing modifies the STO chemical composition, transforming nominally

TiO_2- terminated to SrO-enriched surface. Utilizing ARPES along with the first principal (DFT) calculations disclosed that the formed Sr-enriched STO (001) surface is characterized by the intrinsic splitting of the t_{2g} states while the d_{xy} surface state yields a pure 2D electronic structure. The further UHV annealing at moderate temperature eradicates Sr from the surface and causes the Lifshitz-like transition in the surface band structure (from one band to three bands metallicity).

Our work describes a straightforward method for varying the surface chemical composition, which, combined with VUV-irradiation, efficiently modulates the electronic structures of the t_{2g} band, doping, and electron-phonon interaction in STO. Importantly, the created single-band 2D electronic phase is air-stable (see Supporting Information, Sec. II), showing the potential to serve in designing novel devices. Indeed, the single-band 2DEG states and a light-controlled band splitting in STO offer a new platform for technological applications such as realizing the pure quantum well states in oxides for optoelectronic purposes.

4. Experimental Section

Sample Preparation: In this study, as-received commercially available 0.5% Nb doped nominally TiO_2-terminated $SrTiO_3$ wafers (SurfaceNet GmbH) were used with a miscut within 0.2° to the nominal (001) surface.

During ARPES measurements, multiple surface engineering procedures were applied to the as-received STO wafer, including sputtering and annealing. The sputtering process was conducted under an argon atmosphere with a pressure of 2×10^{-6} mbar at room temperature. The voltage was set as 1 kV and a current of 50 uA for 200–300 s. The STO wafers were 45° facing the ion beam. The vacuum annealing process was conducted under an ultra-high vacuum better than 2×10^{-8} mbar. The annealing temperatures were read through an infrared thermometer. The detailed sample treatment routes were shown in Supporting Information, Sec. I. In this studies, similar results of band modulation in at least another three samples was reproduced, which were shown in Supporting Information Sec. VII.

Angle-Resolved Photoemission Spectroscopy: All the ARPES and XPS data presented were measured at the ULTRA endstation at the Surface/Interface Spectroscopy (SIS) beamline of the Swiss Light Source. The data were acquired with a Scienta Omicron DA30L hemispherical analyzer. The energy and angular resolution were better than 20 meV and 0.1°. The measurements were performed at a temperature of 20 K in a base pressure better than 1×10^{-10} Torr. The unirradiated results were measured by moving the samples to unirradiated areas.

DFT Calculation: The density functional theory calculations were performed within the Perdew–Burke–Ernzehof generalized gradient approximation (PBE-GGA),[49] using the projector augmented wave (PAW) potentials,[50] as implemented in the Vienna ab initio Simulation Package (VASP).[51,52] In addition, the DFT+U functional of Liechtenstein et al.[53] was employed with U = 5 eV and J = 0.64 eV, as similarly performed in reference.[37] A basis set of 500 eV was used, and the structures were relaxed until the forces on atoms were less than 0.01 eVÅ^{-1}. The relaxation of the atomic positions was done using a $4 \times 4 \times 1$ k-mesh, whereas the band structures were evaluated using an $8 \times 8 \times 2$ k-points set.

Supporting Information

Supporting Information is available from the Wiley Online Library or from the author.

Acknowledgements

This work was supported by the Swiss National Science Foundation (SNF), No. 200021_182695 and No. 200021_188413. N.P. acknowledges funding from Villum Fonden for the NEED project (grant No 00027993), the Danish Council for Independent Research Technology and Production Sciences for the DFF- Research Project 3 (grant No 00069B), the support from the "Challenge Programme 2021 – Smart Nanomaterials for Applications in Life-Science" Grant No.NNF21OC0066526 and the fundings received from the ERC Advanced "NEXUS" Grant 101054572. W.H.B acknowledges the support from the Brazilian agencies CNPq, FAPEMIG, and CAPES, as well as the CENAPAD-SP, CESUP (UFRGS), and the National Laboratory for Scientific Computing (LNCC/MCTI, Brazil) for providing HPC resources of the SDumont supercomputer, which have contributed to the research results, URL: http://sdumont.lncc.br. D.V.C. acknowledges the support of Novo Nordisk Foundation NERD Programme: New Exploratory Research and Discovery, Superior Grant NNF21OC0068015.

Open access funding provided by ETH-Bereich Forschungsanstalten.

Author Contributions

M.R. designed the concept and experiments with N.P. and H.L. H.L., E.B.G. A.C. and M.R. performed the ARPES experiment with the help from R.T.D., N.C.P. and M.S. W.H.B. performed the DFT calculations. H. L. processed the ARPES data. H.L. and M.R. wrote the manuscript assisted by E.B.G and A.C and with the help and useful discussions with all other authors.

Conflict of Interest

The authors declare no conflict of interest.

Data Availability Statement

The data that support the findings of this study are available from the corresponding author upon reasonable request.

Keywords

angle-resolved photoemission spectroscopy, surface preparations, SrTiO3, two-dimensional electron gas

Received: November 19, 2022
Revised: February 1, 2023
Published online: February 28, 2023

[1] N. Reyren, S. Thiel, A. D. Caviglia, L. Fitting Kourkoutis, G. Hammerl, C. Richter, C. W. Schneider, T. Kopp, A.-S. Rüetschi, D. Jaccard, M. Gabay, D. A. Muller, J. M. Triscone, J. Mannhart, *Science* **2007**, *317*, 1196.
[2] A. D. Caviglia, S. Gariglio, N. Reyren, D. Jaccard, T. Schneider, M. Gabay, S. Thiel, G. Hammerl, J. Mannhart, J. M. Triscone, *Nature* **2008**, *456*, 624.
[3] A. Joshua, S. Pecker, J. Ruhman, E. Altman, S. Ilani, *Nat. Commun.* **2012**, *3*, 1129.
[4] G. E. D. K. Prawiroatmodjo, F. Trier, D. V. Christensen, Y. Chen, N. Pryds, T. S. Jespersen, *Phys. Rev. B* **2016**, *93*, 184504.

[5] G. Herranz, G. Singh, N. Bergeal, A. Jouan, J. Lesueur, J. Gazquez, M. Varela, M. Scigaj, N. Dix, F. Sanchez, J. Fontcuberta, *Nat. Commun* **2015**, *6*, 6028.
[6] A. Brinkman, M. Huijben, M. van Zalk, J. Huijben, U. Zeitler, J. C. Maan, W. G. van der Wiel, G. Rijnders, D. H. Blank, H. Hilgenkamp, *Nat. Mater.* **2007**, *6*, 493.
[7] B. Kalisky, J. A. Bert, B. B. Klopfer, C. Bell, H. K. Sato, M. Hosoda, Y. Hikita, H. Y. Hwang, K. A. Moler, *Nat. Commun.* **2012**, *3*, 922.
[8] F. Bi, M. Huang, S. Ryu, H. Lee, C. W. Bark, C. B. Eom, P. Irvin, J. Levy, *Nat. Commun.* **2014**, *5*, 5019.
[9] D. V. Christensen, Y. Frenkel, Y. Z. Chen, Y. W. Xie, Z. Y. Chen, Y. Hikita, A. Smith, L. Klein, H. Y. Hwang, N. Pryds, B. Kalisky, *Nat. Phys.* **2019**, *15*, 269.
[10] A. D. Caviglia, M. Gabay, S. Gariglio, N. Reyren, C. Cancellieri, J.-M. Triscone, *Phys. Rev. Lett.* **2010**, *104*, 126803.
[11] Y. Gan, Y. Zhang, D. V. Christensen, N. Pryds, Y. Chen, *Phys. Rev. B* **2019**, *100*, 125134.
[12] F. Trier, G. E. D. K. Prawiroatmodjo, Z. Zhong, D. V. Christensen, M. von Soosten, A. Bhowmik, J. M. G. Lastra, Y. Chen, T. S. Jespersen, N. Pryds, *Phys. Rev. Lett.* **2016**, *117*, 096804.
[13] Y. Matsubara, K. S. Takahashi, M. S. Bahramy, Y. Kozuka, D. Maryenko, J. Falson, A. Tsukazaki, Y. Tokura, M. Kawasaki, *Nat. Commun.* **2016**, *7*, 11631.
[14] N. C. Plumb, M. Salluzzo, E. Razzoli, M. Månsson, M. Falub, J. Krempasky, C. E. Matt, J. Chang, M. Schulte, J. Braun, H. Ebert, J. Minár, B. Delley, K.-J. Zhou, T. Schmitt, M. Shi, J. Mesot, L. Patthey, M. Radović, *Phys. Rev. Lett.* **2014**, *113*, 086801.
[15] Y. Z. Chen, N. Bovet, F. Trier, D. V. Christensen, F. M. Qu, N. H. Andersen, T. Kasama, W. Zhang, R. Giraud, J. Dufouleur, T. S. Jespersen, J. R. Sun, A. Smith, J. Nygård, L. Lu, B. Büchner, B. G. Shen, S. Linderoth, N. Pryds, *Nat. Commun.* **2013**, *4*, 1371.
[16] A. Chikina, D. V. Christensen, V. Borisov, M. A. Husanu, Y. Chen, X. Wang, T. Schmitt, M. Radovic, N. Nagaosa, A. S. Mishchenko, R. Valentí, N. Pryds, V. N. Strocov, *ACS Nano* **2021**, *15*, 4347.
[17] Y. Gan, D. V. Christensen, Y. Zhang, H. Zhang, D. Krishnan, Z. Zhong, W. Niu, D. J. Carrad, K. Norrman, M. von Soosten, T. S. Jespersen, B. Shen, N. Gauquelin, J. Verbeeck, J. Sun, N. Pryds, Y. Chen, *Adv. Mater.* **2019**, *31*, 1805970.
[18] A. F. Santander-Syro, F. Fortuna, C. Bareille, T. C. Rödel, G. Landolt, N. C. Plumb, J. H. Dil, M. Radović, *Nat. Mater.* **2014**, *13*, 1085.
[19] E. B. Guedes, S. Muff, M. Fanciulli, A. P. Weber, M. Caputo, Z. Wang, N. C. Plumb, M. Radovic, J. H. Dil, *Phys. Rev. Research* **2020**, *3*, 033173.
[20] Z. Salman, R. F. Kiefl, K. H. Chow, M. D. Hossain, T. A. Keeler, S. R. Kreitzman, C. D. P. Levy, R. I. Miller, T. J. Parolin, M. R. Pearson, H. Saadaoui, J. D. Schultz, M. Smadella, D. Wang, W. A. MacFarlane, *Phys. Rev. Lett.* **2006**, *96*, 147601.
[21] M. Smadella, Z. Salman, K. Chow, M. Egilmez, I. Fan, M. Hossain, R. Kiefl, S. Kreitzman, C. Levy, W. MacFarlane, A. Mansour, G. Morris, T. Parolin, M. Pearson, H. Saadaoui, Q. Song, D. Wang, *Phys. B: Cond Matter* **2009**, *404*, 924.
[22] Z. Salman, M. Smadella, W. A. MacFarlane, B. D. Patterson, P. R. Will-mott, K. H. Chow, M. D. Hossain, H. Saadaoui, D. Wang, R. F. Kiefl, *Phys. Rev. B* **2011**, *83*, 224112.
[23] E. B. Guedes, S. Muff, W. H. Brito, M. Caputo, H. Li, N. C. Plumb, J. H. Dil, M. Radović, *Adv. Sci.* **2021**, *8*, 2100602.
[24] B. Burganov, C. Adamo, A. Mulder, M. Uchida, P. D. C. King, J. W. Harter, D. E. Shai, A. S. Gibbs, A. P. Mackenzie, R. Uecker, M. Bruetzam, M. R. Beasley, C. J. Fennie, D. G. Schlom, K. M. Shen, *Phys. Rev. Lett.* **2016**, *116*, 197003.
[25] B. Jalan, S. J. Allen, G. E. Beltz, P. Moetakef, S. Stemmer, *Appl. Phys. Lett.* **2011**, *98*, 132102.
[26] E. B. Guedes, T. W. Jensen, M. Naamneh, A. Chikina, R. T. Dahm, S. Yun, F. M. Chiabrera, N. C. Plumb, J. H. Dil, M. Shi, D. V. Christensen, W. H. Brito, N. Pryds, M. Radović, *J. Vac. Sci. Technol. A* **2022**, *40*, 013213.
[27] S. N. Rebec, T. Jia, H. M. Sohail, M. Hashimoto, D. Lu, Z.-X. Shen, R. G. Moore, *Proc. Natl. Acad. Sci. U.S.A.* **2019**, *116*, 16687.
[28] E. B. Guedes, S. Muff, M. Fanciulli, A. P. Weber, M. Caputo, Z. Wang, N. C. Plumb, M. Radović, J. H. Dil, *Phys. Rev. Res.* **2020**, *2*, 033173.
[29] M. Radović, N. Lampis, F. M. Granozio, P. Perna, Z. Ristic, M. Salluzzo, C. M. Schlepütz, U. Scotti di Uccio, *Appl. Phys. Lett.* **2009**, *94*, 022901.
[30] A. Chikina, F. Lechermann, M. A. Husanu, M. Caputo, C. Cancellieri, X. Wang, T. Schmitt, M. Radovic, V. N. Strocov, *ACS Nano* **2012**, *12*, 7927.
[31] A. F. Santander-Syro, O. Copie, T. Kondo, F. Fortuna, S. Pailhès, R. Weht, X. G. Qiu, F. Bertran, A. Nicolaou, A. Taleb-Ibrahimi, P. L. Fèvre, G. Herranz, M. Bibes, N. Reyren, Y. Apertet, P. Lecoeur, A. Barthélémy, M. J. Rozenberg, *Nature* **2011**, *469*, 189.
[32] W. Meevasana, P. D. C. King, R. H. He, S.-K. Mo, M. Hashimoto, A. Tamai, P. Songsiriritthigul, F. Baumberger, Z.-X. Shen, *Nat. Mater.* **2011**, *10*, 114.
[33] N. C. Plumb, M. Kobayashi, M. Salluzzo, E. Razzoli, C. E. Matt, V. N. Strocov, K. J. Zhou, M. Shi, J. Mesot, T. Schmitt, L. Patthey, M. Radović, *Appl. Surf. Sci.* **2017**, *412*, 271.
[34] X. Yan, F. Wrobel, I. Tung, H. Zhou, H. Hong, F. Rodolakis, A. Bhattacharya, J. L. McChesney, D. D. Fong, *Adv. Mater.* **2022**, *34*, 2200866.
[35] H. K. Yoo, L. Moreschini, A. Bostwick, A. L. Walter, T. W. Noh, E. Rotenberg, Y. J. Chang, *Curr. Appl. Phys.* **2020**, *20*, 1268.
[36] F. V. E. Hensling, C. Baeumer, M. Rose, F. Gunkel, R. Dittmann, *Mater. Res. Lett.* **2020**, *8*, 31.
[37] J. Shen, H. Lee, R. Valentí, H. O. Jeschke, *Phys. Rev. B* **2012**, *86*, 195119.
[38] P. Delugas, V. Fiorentini, A. Mattoni, A. Filippetti, *Phys. Rev. B* **2015**, *91*, 115315.
[39] T. Ando, A. B. Fowler, F. Stern, *Rev. Mod. Phys.* **1982**, *54*, 437.
[40] K. Ueno, S. Nakamura, H. Shimotani, A. Ohtomo, N. Kimura, T. Nojima, H. Aoki, Y. Iwasa, M. Kawasaki, *Nat. Mater.* **2008**, *7*, 855.
[41] D. V. Christensen, Y. Frenkel, P. Schütz, F. Trier, S. Wissberg, R. Claessen, B. Kalisky, A. Smith, Y. Z. Chen, N. Pryds, *Phys. Rev. Appl.* **2018**, *9*, 054004.
[42] C. Chen, J. Avila, E. Frantzeskakis, A. Levy, M. C. Asensio, *Nat. Commun.* **2014**, *6*, 8585.
[43] Z. Wang, S. McKeown Walker, A. Tamai, Y. Wang, Z. Ristic, F. Y. Bruno, A. de la Torre, S. Riccò, N. C. Plumb, M. Shi, P. Hlawenka, J. Sánchez-Barriga, A. Varykhalov, T. K. Kim, M. Hoesch, P. D. C. King, W. Meevasana, U. Diebold, J. Mesot, B. Moritz, T. P. Devereaux, M. Radovic, F. Baumberger, *Nat. Mater.* **2016**, *15*, 835.
[44] C. Cancellieri, A. S. Mishchenko, U. Aschauer, A. Filippetti, C. Faber, O. S. Barišić, V. A. Rogalev, T. Schmitt, N. Nagaosa, V. N. Strocov, *Nat. Commun.* **2016**, *7*, 10386.
[45] H. Fröhlich, H. Pelzer, S. Zienau, *Phil. Mag.* **1950**, *41*, 221.
[46] J. T. Devreese, A. S. Alexandrov, *Rep. Prog. Phys.* **2009**, *72*, 066501.
[47] A. S. Mishchenko, N. V. Prokof'ev, A. Sakamoto, B. V. Svistunov, *Phys. Rev. B* **2000**, *62*, 6317.
[48] R. P. Feynman, *Phys. Rev.* **1955**, *92*, 660.
[49] J. P. Perdew, K. Burke, M. Ernzerhof, *Phys. Rev. Lett.* **1996**, *77*, 3865.
[50] P. E. Blüchl, *Phys. Rev. B* **1994**, *50*, 17953.
[51] G. Kresse, J. Furthmüller, *Comput. Mater. Sci.* **1996**, *6*, 15.
[52] G. Kresse, J. Furthmüller, *Phys. Rev. B* **1996**, *54*, 11169.
[53] A. I. Liechtenstein, V. I. Anisimov, J. Zaanen, *Phys. Rev. B* **1995**, *52*, R5467.